Micromagnetometry of two-dimensional ferromagnets

Citation for published version (APA):
Kim, M., Kumaravadivel, P., Birkbeck, J., Kuang, W., Xu, S., Hopkinson, D. G., Knolle, J., Mcclarty, P. A., Berdyugin, A. I., Ben Shalom, M., Gorbachev, R. V., Haigh, S. J., Liu, S., Edgar, J. H., Novoselov, K. S., Grigorieva, I. V., & Geim, A. K. (2019). Micromagnetometry of two-dimensional ferromagnets. *Nature Electronics*. https://doi.org/10.1038/s41928-019-0302-6

Citing this paper
Please note that where the full-text provided on Manchester Research Explorer is the Author Accepted Manuscript or Proof version this may differ from the final Published version. If citing, it is advised that you check and use the publisher's definitive version.

Micromagnetometry of two-dimensional ferromagnets

M. Kim[1*], P. Kumaravadivel[1,2*], J. Birkbeck[1,2], W. Kuang[1], S. G. Xu[1,2], D. G. Hopkinson[3], J. Knolle[4], P. A. McClarty[5], A. I. Berdyugin[1], M. Ben Shalom[1,2], R. V. Gorbachev[1,2], S. J. Haigh[3], S. Liu[6], J. H. Edgar[6], K. S. Novoselov[1,2], I. V. Grigorieva[1], A. K. Geim[1,2*]

[1]School of Physics and Astronomy, University of Manchester, Oxford Road, Manchester, M13 9PL, United Kingdom

[2]National Graphene Institute, University of Manchester, Oxford Road, Manchester, M13 9PL, United Kingdom

[3]School of Materials, University of Manchester, Oxford Road, M13 9PL, United Kingdom

[4]Blackett Laboratory, Imperial College London, London SW7 2AZ, United Kingdom

[5]Max Planck Institute for the Physics of Complex Systems, Nöthnitzer Strasse 38, 01187 Dresden, Germany

[6]The Tim Taylor Department of Chemical Engineering, Kansas State University, Manhattan, Kansas 66506, USA

[*]Correspondence and requests for materials should be addressed to
M.K. (minsoo.kim@manchester.ac.uk), P.K. (piranavan.kumaravadivel@manchester.ac.uk) or A.K.G. (geim@manchester.ac.uk).

The study of atomically-thin ferromagnetic crystals has led to the discovery of unusual magnetic behaviour and provided insight into the magnetic properties of bulk materials. However, the experimental techniques that were used to explore two-dimensional ferromagnetism could not probe the magnetic field directly. Here we show that ballistic Hall micromagnetometry provides a reliable and convenient way to measure magnetization of individual two-dimensional ferromagnets. Our devices are made by van der Waals assembly in such a way that the investigated ferromagnetic crystal is placed on top of a multiterminal Hall bar made from encapsulated graphene. We apply the micromagnetometry to study atomically-thin chromium tribromide (CrBr$_3$). The material remains ferromagnetic down to monolayer thickness and exhibits strong out-of-plane anisotropy. Magnetic response of CrBr$_3$ varies little with the number of layers and its temperature dependence cannot be described by the simple Ising model of two-dimensional ferromagnetism.

Probing magnetism in layered van der Waals (vdW) crystals[1-9] has revealed a range of interesting phenomena including unexpected changes in magnetic properties as a function of the number of layers[2,10] and the possibility to control magnetism by electric and chemical doping[11-16]. Ferromagnetic semiconductors[17], such as Cr$_2$Ge$_2$Te$_6$, CrI$_3$ and CrBr$_3$, are of particular interest because of their magnetization-dependent optical response and electrical switching of magnetization direction[11-15]. To study the magnetic properties of these two-dimensional (2D) materials, a variety of different techniques have been employed, including the magneto-optical Kerr effect[1,2,14], circular dichroism microscopy[11,13], tunnel magnetoresistance[3-6,15], the anomalous Hall effect[7], photoluminescence[8,18] and Raman spectroscopy[9]. However, none of these techniques can probe the magnetic field response directly, which could be used to extract further information about, for example, phase transitions, spin arrangements, domain structures and magnetic walls' movements. Conventional magnetometry techniques, which were developed to study the magnetic response of bulk materials, are also

unsuitable for these 2D materials because of the size of the crystals involved (only a few atoms thick and, typically, only several micrometres across)[10].

The Hall micromagnetometry technique, which was initially developed to study mesoscopic superconductors and ferromagnets, employs small Hall probes to measure the magnetic response from an object placed in vicinity of the probes[19,20]. In particular, the measured Hall resistance is given by the total magnetic flux through the central (square) area of the Hall cross, if charge carriers move through the area without scattering, that is, if electron transport is ballistic. Under this condition, the technique allows not just qualitative observations but quantitative analysis of the measured magnetization signals. Early Hall magnetometers were made of high-mobility 2D electron gases using, typically, GaAlAs heterostructures. Recent progress in the fabrication of vdW heterostructures means that the approach can now be extended to 2D magnetic crystals in combination with the use of Hall probes made from high-quality graphene.

In this Article, we report the use of graphene-based ballistic Hall micromagnetometry[19] to study the magnetization of individual 2D ferromagnets. Our devices are multilayer vdW heterostructures[21] in which a ferromagnetic crystal (e.g., atomically-thin $CrBr_3$) protected by its encapsulation between two hexagonal boron nitride (hBN) crystals is placed on top of a Hall bar made from encapsulated graphene[22]. The use of encapsulated graphene ensures high-sensitivity and low-noise measurements, due to the nanometre-scale proximity of the 2D ferromagnet to the high-mobility conducting channel that allows ballistic electron transport up to room temperature[23]. We find that the temperature dependence of magnetization varies little with the $CrBr_3$ thickness, indicating the strongly-layered nature of the ferromagnetic material. We also explore domain walls' propagation in such atomically-thin ferromagnets and, to highlight the generality of our approach, use the Hall micromagnetometry to study another 2D magnetic material, $Cr_2Ge_2Te_6$.

Graphene-based Hall micromagnetometry of 2D ferromagnets
Our Hall bar devices (Fig. 1a) were prepared by encapsulating graphene within hBN using the standard dry transfer method (see Methods). The mesa and electrical contacts were fabricated using electron-beam lithography, dry etching and thin-film metal deposition. The ferromagnetic crystal was mechanically exfoliated in a glovebox filled with pure argon and, to avoid chemical degradation in air[22], sandwiched between a pair of thin hBN crystals inside the oxygen- and water- free atmosphere. This trilayer assembly was then transferred on top of the graphene device so that the 2D ferromagnet covered at least one of the Hall crosses as shown in Fig. 1a (below we refer to such crosses as 'ferromagnet' ones). Each device had some Hall crosses left uncovered to be used as references.

Special precautions were taken to ensure that it was possible to replace a studied 2D crystal with another one, after a measurement programme was complete. To this end, the crystals were placed on top of Hall bars in such a way that a part of the encapsulating hBN extended over the gold contact leads (see Figs 1a,b). Weak adhesion between hBN and Au then ensured the possibility to peel off the trilayer assembly and replace it with another encapsulated 2D ferromagnet. With these arrangements in place, it was possible to repeatedly replace 2D crystals and study them without degradation in sensitivity of our Hall-bar devices (Fig. 1b and Supplementary Fig. 1).

We focus below on magnetic properties of 2D $CrBr_3$, which was chosen primarily because of its high environmental stability as compared to other magnetic 2D materials (for example, CrI_3; see Supplementary Fig. 2)[24]. Indeed, our encapsulated $CrBr_3$ samples remained stable for at least several months without any sign of degradation (Supplementary Fig. 3). However, to emphasize the generality of the reported approach, we also present experimental results obtained when the micromagnetometry was applied to 2D $Cr_2Ge_2Te_6$ (Supplementary Fig. 4).

An example of basic characterization of our graphene Hall bar devices is provided in Fig. 1c that shows their longitudinal resistivity (ρ_{xx}) and Hall coefficient (α_H) as a function of gate voltage (V_{bg}). The devices were ~2 μm in width and exhibited typical carrier mobilities of ~200,000 $cm^2 V^{-1} s^{-1}$, which ensured ballistic transport over a wide temperature (T) range. Our experiments followed the same methodology as described previously[19,20]. First, we limited the measurements to magnetic fields below ~0.1 T where the cyclotron radius was larger than the size of our Hall crosses so that the Hall response was linear in field. Next, we analysed the sensitivity of Hall crosses at different V_{bg} and found that it was maximal for concentrations of ~10^{12} cm^{-2} as indicated in Fig. 1c. The Hall responses of the ferromagnet and reference crosses are given[19,20] by $R_H^{FM} = \alpha_H \cdot (\mu_0 H + B)$ and $R_H^{ref} = \alpha_H \cdot \mu_0 H$, respectively, where $\mu_0 H$ is the externally applied field and B is the average magnetic field within the flux sensitive area (FSA) of a ballistic Hall cross, which is indicated by the dotted black lines in Fig. 2. The differential amplifier scheme shown in Fig. 1a allowed direct measurements of $\Delta = R_H^{FM} - R_H^{ref}$. Because the α_H (that depends on V_{bg}) is known experimentally, the found $\Delta = \alpha_H B$ yields directly B. Nonetheless, different Hall crosses are always slightly different because of minute changes in geometry and mesoscopic (interference) effects. This leads to non-zero $\Delta(H)$ even for nominally similar Hall crosses and in the absence of a ferromagnet on top. To suppress this spurious but smooth background (see Fig. 2a), we used high driving currents of the order of 100 μA, which raised electron temperature in graphene and reduced mesoscopic effects but did not heat the nearby 2D ferromagnet[19,20]. In addition, we measured $\Delta(H)$ at T above the ferromagnetic transition (typically at 40 K for the case of $CrBr_3$; see Methods) and subtracted it from low-T Δ, which allowed us to obtain clean B signals such as those shown in Figs. 2b-d. The achieved resolution in terms of B was about 1 μT, which translates into ~10^{-3} of the magnetic flux quantum. Finally, it is important to note that, because of demagnetization effects, the stray fields from 2D ferromagnets exhibit sharp spikes near their edges, which can reach a value of several mT (Supplementary Fig. 5). This strength is far too small to result in cyclotron orbits within the sub-100 nm extent of the regions and, therefore, the use of the Hall signal as a quantitative measure of the average magnetic flux within the FSA holds[19,20]. Moreover, the spikes are sign changing so that on average they have little effect on passing electrons. Accordingly, it is the interior regions of the 2D ferromagnets rather than edges, which contribute mostly to the measured Hall effect, as confirmed by our micromagnetic simulations.

Magnetization behaviour of atomically-thin $CrBr_3$

All the studied $CrBr_3$ samples exhibited clear magnetic hysteresis at low T, and the switching field H required to reach the saturation state was typically a few tens of mT (Fig. 2). The value of B at saturation is directly proportional to the magnetization M of a 2D ferromagnet with the proportionality coefficient given by demagnetization effects[25]. This coefficient depends on the shape and size of the measured crystal and can accurately be evaluated using micromagnetic simulations (Methods). Results of such simulations are shown in Figs. 2a-d for the specific crystals under investigation. From the saturation value of B we estimated the magnetization per chromium atom,

which is found to be 3.6 $\pm$0.2 μ_B for all the studied 2D CrBr$_3$ samples, independently of their thickness (right axes in Figs. 2b-d). This value is in good agreement with 3.8 μ_B per Cr atom for bulk CrBr$_3$, which was found using large crystals and a commercial SQUID magnetometer (Supplementary Fig. 6). The agreement corroborates the high quality of encapsulated 2D CrBr$_3$ and the absence of degradation. Importantly, the fact that the remanent magnetization per Cr atom did not depend on the number of layers also proved that spins in different CrBr$_3$ layers had the same (ferromagnetic) alignment, in contrast to the behavior[2-4,6] observed for 2D CrI$_3$ where adjacent layers exhibited antiferromagnetism.

The observed hysteresis loops in Fig. 2 exhibit a complex structure, which is particularly profound for the crystal in Fig. 2c where large jumps result in values of B that reach well above the value of the fully spin-polarized state (regions III and IV). The circulation of the resulting (smaller) hysteresis loops is opposite to normal. This counterintuitive behaviour is attributed to the formation of magnetic domains within CrBr$_3$, which can result in a larger flux through the FSA despite the net magnetization of the entire 2D ferromagnetic crystal is smaller. Indeed, our micromagnetic simulations show that, if a domain wall is located near an edge of the FSA (states III and IV in Fig. 2c), the average flux inside the area notably increases with respect to that for states I and II because of weaker demagnetization effects for the two-domain configuration. As the applied field changes further, the domain wall moves away from the FSA region so that crystal's spin polarization gets reversed and B decreases to its normal fully-polarized value determined by the crystal's shape. Similar 'opposite-circulation' loops were observed for other 2D CrBr$_3$ crystals, although they were usually smaller (e.g., Fig. 2d). This is not surprising as the loop size is determined by specific domain arrangements with respect to the FSA. In addition, the hysteresis loops always exhibited many small steps such as those seen clearly for the monolayer crystal in Fig. 2b. These are Barkhausen steps that appear because domain walls propagate across the Hall cross through a series of pinned states[26]. For completeness, Fig. 3 shows partial hysteresis loops for the monolayer CrBr$_3$. In this case, we reversed the sweep direction after a domain wall appeared within the FSA, which allowed us to stabilize the wall in several pinned positions.

2D ferromagnetism in CrBr$_3$ and anomalous scaling

Below we examine how magnetization of 2D CrBr$_3$ depends on T. Figure 4a shows hysteresis curves found for monolayer CrBr$_3$ at different T. The coercivity rapidly diminishes with increasing T and vanishes above 20 K. Despite the disappearance of hysteresis, a finite magnetization step near zero H persisted to higher T, up to ~27 K for the case of monolayer CrBr$_3$. This step indicates the magnetization reversal. For quantitative analysis, we determined the saturation magnetization M_s from the experimental curves using the procedure illustrated in the inset of Fig. 4a. Figure 4b plots the T dependence of M_s for monolayer CrBr$_3$. Such plots allowed accurate estimation of the critical (Curie) temperature T_c and, also, more precise evaluation of low-T M_s as compared to the procedure using single-temperature sweeps in Fig. 2. Figure 4c shows T_c as a function of the number N of CrBr$_3$ layers. The critical temperature gradually decreases from ~36 K for bulk crystals to ~27 K for the monolayer. The relatively small decrease in T_c with decreasing thickness suggests that interlayer magnetic interactions in CrBr$_3$ are weak so that, in the first approximation, the bulk compound can be considered simply as a stack of ferromagnetic monolayers.

Empirically, the observed $M_s(T)$ follow the power law $(1-T/T_c)^\beta$ with the best fit yielding the exponent $\beta \approx 0.4 \pm 0.1$ for monolayer CrBr$_3$ (Fig. 4b; Supplementary Fig. 7). Within our experimental accuracy, all the studied CrBr$_3$ samples exhibited the same β, independently of the number of layers. This value

also agrees with $\beta \approx 0.37$ for bulk $CrBr_3$ as found previously[27]. On one hand, the observation of the N-independent critical exponent β seems logical. Indeed, for a strongly layered material in which ferromagnetism weakly evolves with the number of layers as in $CrBr_3$, $M(T)$ should also change little with N. On the other hand, strictly-2D ferromagnetism with out-of-plane magnetization is generally described by the Ising model that yields much smaller $\beta = 0.125$ because temperature is less efficient in creating excitations in the 2D space[28]. Such a small exponent matches our data poorly, especially close to T_c where the critical power law scaling behaviour should be valid (Fig. 4b; Supplementary Fig. 7). To address the observed disparity, we refer to the work[29] on monolayer CrI_3, a sister compound of $CrBr_3$, in which it was suggested that an XXZ model with perturbing bond-dependent Kitaev interactions could be more appropriate to describe magnetic interactions in these layered compounds that are not dissimilar to $RuCl_3$, an archetypal example of a spin liquid[30]. We find that our magnetization data over the entire T range are indeed well described by a mean-field calculation for the above XXZ model (blue curve, Fig 4b). It yields $\beta = 0.5$ at criticality, a value that agrees with the experiment, too (Supplementary Fig. 7). Further work is required to establish the exact nature of magnetic interactions in $CrBr_3$ and whether they indeed lead to mean-field behaviour. From this perspective, it is important to mention that, above 20 K, the magnetization loops for 2D $CrBr_3$ are no longer rectangular, and the remanent magnetization M_r is somewhat smaller than M_s (inset of Fig. 4a). This reduction in zero-field magnetization is presumably caused by spontaneous micro-domain formation. To this end, we also measured $M_r(T)$ but found that it was described by the same β as M_s.

Finally, we studied how hysteresis loops in the 2D ferromagnet changed in tilted magnetic fields (Fig. 5). Interestingly, both M_s and M_r were found to be practically independent of the in-plane field component $H_\parallel$, which corroborates the high uniaxial anisotropy of $CrBr_3$ even in its monolayer form. At the same time, the perpendicular component $H_\perp$ of the external field, which was required to flip the spin polarization, was notably reduced with increasing the tilt angle θ (Fig. 5a). The likely explanation for the latter behaviour is that the in-plane field helps reduce the energy barrier for nucleation of domains of opposite polarity.

Conclusions
Ballistic Hall micromagnetometry is a powerful tool for investigation of 2D ferromagnetic materials, allowing quantitative studies of their magnetization behaviour. The same graphene-based Hall device can be used repeatedly to study ferromagnetic samples of different materials, thicknesses, shapes and sizes, highlighting the convenience and reliability of the technique. The Hall micromagnetometry can also be used to investigate details of nucleation and propagation of domain walls, as well as their pinning mechanisms in 2D.

Methods

Device fabrication. The Hall devices were made from graphene encapsulated between two hBN crystals using the standard dry transfer technique and polypropylene carbonate (PPC) coated polydimethylsiloxane (PDMS) films as stamps. The hBN crystals used in this work were produced by the atmospheric pressure metal-flux method[31]. The metal contacts (5 nm Cr/ 50-70 nm Au) and the Hall bar mesa were fabricated as in the previous reports[32,33]. The only notable difference with respect to the earlier procedures was that, to define the mesa, we etched narrow trenches (100 - 200 nm wide) whereas the rest of the hBN/graphene/hBN stack was kept intact. Also, the thickness of the contact metallization was deliberately chosen close to that of the hBN/graphene/hBN stack. This made the surface of our devices mostly flush to facilitate successive transfers of 2D $CrBr_3$ crystals.

The encapsulated $CrBr_3$ samples were prepared in an argon-filled glovebox with levels of O_2 and H_2O below 0.5 ppm. First, bulk $CrBr_3$ (*HQ Graphene*) was exfoliated onto a clean SiO_2/Si substrate. Although we could use bare SiO_2/Si substrates, a thin (7 nm) Au coating was found to increase the probability of finding mono- and bi- layer crystals of $CrBr_3$, in agreement with the earlier work on another layered ferromagnet[7]. Crystals' thickness was first estimated by optical contrast. Then, using a PPC-coated PDMS stamp, a selected $CrBr_3$ crystal was encapsulated between two hBN crystals that were typically 20-40 nm thick. Once encapsulated, the thickness of 2D $CrBr_3$ was verified by atomic force microscopy. Next, again using the argon atmosphere, the encapsulated $CrBr_3$ attached to a PDMS/PPC stamp was aligned and released onto one (or two) of the Hall crosses[34]. The other crosses within the Hall bar devices were left bare for reference measurements. After this, the device was ready for electrical measurements. The etched trenches and weak adhesion between encapsulated $CrBr_3$ and the gold electrodes enabled us to easily peel the $CrBr_3$ stack off the electrode-clamped Hall bar (using PPC/PDMS stamps again) so that $CrBr_3$ of a different thickness can be placed on top of the same Hall magnetometer. Note that the out-of-plane field emerging from a 2D ferromagnet weakens at distances comparable to the lateral size of magnetic domains. The use of relatively thin hBN spacers ensured that we could detect small movements of domains of only tens nm in size, as illustrated in the inset of Fig. 3.

Transmission electron microscopy. Thin $CrBr_3$ was mechanically exfoliated and then encapsulated between two monolayer graphene flakes using the same dry-peel transfer procedures as described above. High angle annular dark field (HAADF) imaging was carried out in a double aberration-corrected JEOL ARM300F with a cold field emission electron gun operating at 80 keV, with a beam convergence semi-angle of 31.74 mrad and HAADF detection range of 68-206 mrad. All aberrations were corrected to better than a $\pi/4$ phase shift at 30 mrad.

Measurements of magnetic hysteresis. Hall measurements were performed using the standard lock-in technique at a finite V_{bg} away from the charge neutrality point, where graphene displayed high carrier mobility and, at the same time, strong Hall response. To capture full magnetic hysteresis curves, the Hall resistance was measured at a fixed sensitivity of the lock-in amplifier (Stanford Research Systems 830) while sweeping H to above the switching field. Because the detected B were typically < 0.1% of the switching field, the resolution of digital lock-in amplifiers was insufficient to detect the resulting small changes in Hall voltage. Therefore, we measured the difference in Hall voltages of the 'ferromagnet' and reference Hall crosses using two voltage preamplifiers (Fig. 1a), which allowed the reported high-resolution data.

The excitation current I_{ac} were chosen typically in the range from 10 μA to 200 μA. Higher currents improved the resolution of our measurements by reducing noise and mesoscopic fluctuations in graphene but they could also heat up $CrBr_3$. Therefore, an optimal I_{ac} was selected such that it simultaneously minimized heating effects, mesoscopic fluctuations and noise for a given V_{bg}. The devices remained ballistic for all I_{ac}. This careful adjustment of experimental parameters allowed a field resolution of about 1 μT. The above sensitivity is comparable to the highest resolution achieved for Hall micromagnetometers based on GaAs/GaAlAs heterostructures[19,20]. We believe that the field resolution can be further improved by using graphene devices with wider contact regions and, therefore, lower contact resistance that is responsible for noise[35].

Numerical simulations. Using finite-element analysis, we numerically calculated the spatially varying perpendicular field $B(x,y)$ projected by a ferromagnetic crystal into the graphene plane of magnetometers through hBN spacers. To this end, the exact geometry of 2D $CrBr_3$ crystals (Fig. 2b-d) was obtained by atomic force microscopy. Assuming the constant magnetization M in the out-of-plane direction, we used a numerical mesh in the shape of our $CrBr_3$ crystals and calculated the demagnetizing proportionality coefficient between average $B(x,y)$ within the FSA in the graphene plane and M. This coefficient that depended on the shape of the crystal was used to convert the experimentally detected values of B at saturation into M.

Spin-3/2 XXZ-Kitaev model. We computed the spontaneous magnetization within a local mean field theory for this model described by

$$\mathcal{H}_{XXZ-K} = \sum_{\langle i,j \rangle} \left(\frac{J_\perp}{2} \left(S_i^+ S_j^- + S_i^- S_j^+ \right) + J_\parallel S_i^z S_j^z \right) + K \sum_{\langle i,j \rangle_\alpha} S_i^\alpha S_j^\alpha$$

Decoupling the bilinear exchange and solving the self-consistent equation for the local exchange field at finite T, we obtained the average magnetization

$$\langle S_i \rangle = \frac{Tr \left(S_i e^{-\beta \mathcal{H}_{MFT}(i)} \right)}{Z(i)}$$

where $Z(i) = Tr\ e^{-\beta \mathcal{H}_{MFT}(i)}$ with $H_{MFT} = S_i \cdot h_i$. The field h_i is the exchange field from neighboring magnetic sites on the honeycomb lattice. This gives the T dependent magnetization directly. The data do not constrain the parameters of this model except for an overall scale. The corresponding fit in Fig. 4b is for $J_\perp = -5.23$ K, $J_\parallel = -6.33$ K, $K = -1.7$ K and the g-factor $g = 2.2$ defined through $\langle J_{i,Cr} \rangle = g\langle S_i \rangle$.

Data availability
The data that support our findings are available from the corresponding authors upon reasonable request.

Code availability
The computer code used in this study is available from the corresponding authors upon reasonable request.

References

1   Gong, C. et al. Discovery of intrinsic ferromagnetism in two-dimensional van der Waals crystals. *Nature* **546**, 265-269 (2017).

2   Huang, B. et al. Layer-dependent ferromagnetism in a van der Waals crystal down to the monolayer limit. *Nature* **546**, 270-273 (2017).

3   Song, T. et al. Giant tunneling magnetoresistance in spin-filter van der Waals heterostructures. *Science* **360**, 1214-1218 (2018).

4   Klein, D. R. et al. Probing magnetism in 2D van der Waals crystalline insulators via electron tunneling. *Science* **360**, 1218-1222 (2018).

5   Ghazaryan, D. et al. Magnon-assisted tunnelling in van der Waals heterostructures based on $CrBr_3$. *Nat. Electron.* **1**, 344-349 (2018).

6   Wang, Z. et al. Very large tunneling magnetoresistance in layered magnetic semiconductor CrI_3. *Nat. Commun*. **9**, 2516 (2018).

7   Fei, Z. et al. Two-dimensional itinerant ferromagnetism in atomically thin Fe_3GeTe_2. *Nat. Mater*. **17**, 778-782 (2018).

8   Seyler, K. L. et al. Ligand-field helical luminescence in a 2D ferromagnetic insulator. *Nat. Phys*. **14**, 277-281 (2018).

9   Yao, T., Mason, J. G., Huiwen, J., Cava, R. J. & Kenneth, S. B. Magneto-elastic coupling in a potential ferromagnetic 2D atomic crystal. *2D Mater*. **3**, 025035 (2016).

10   Burch, K. S., Mandrus, D. & Park, J.-G. Magnetism in two-dimensional van der Waals materials. *Nature* **563**, 47-52 (2018).

11   Jiang, S., Shan, J. & Mak, K. F. Electric-field switching of two-dimensional van der Waals magnets. *Nat*. *Mater*. **17**, 406-410 (2018).

12   Huang, B. et al. Electrical control of 2D magnetism in bilayer CrI_3. *Nat. Nanotechnol*. **13**, 544-548 (2018).

13   Jiang, S., Li, L., Wang, Z., Mak, K. F. & Shan, J. Controlling magnetism in 2D CrI_3 by electrostatic doping. *Nat. Nanotechnol*. **13**, 549-553 (2018).

14   Wang, Z. et al. Electric-field control of magnetism in a few-layered van der Waals ferromagnetic semiconductor. *Nat*. *Nanotechnol*. **13**, 554-559 (2018).

15   Song, T. et al. Voltage control of a van der Waals spin-filter magnetic tunnel junction. *Nano Lett.* **19**, 915-920 (2019).

16   Abramchuk, M. et al. Controlling magnetic and optical properties of the van der Waals crystal $CrCl_{3-x}Br_x$ via mixed halide chemistry. *Adv*. *Mater*. **30**, 1801325 (2018).

17   McGuire, M. Crystal and magnetic Structures in layered, transition metal dihalides and trihalides. *Crystals* **7**, 121 (2017).

18   Zhong, D. et al. Van der Waals engineering of ferromagnetic semiconductor heterostructures for spin and valleytronics. *Sci*. *Adv*. **3**, e1603113 (2017).

19   Geim, A. K. et al. Phase transitions in individual sub-micrometre superconductors. *Nature* **390**, 259-262 (1997).

20   Novoselov, K. S., Geim, A. K., Dubonos, S. V., Hill, E. W. & Grigorieva, I. V. Subatomic movements of a domain wall in the Peierls potential. *Nature* **426**, 812-816 (2003).

21   Geim, A. K. & Grigorieva, I. V. Van der Waals heterostructures. *Nature* **499**, 419-425 (2013).

22   Cao, Y. et al. Quality heterostructures from two-dimensional crystals unstable in air by their assembly in inert atmosphere. *Nano Lett*. **15**, 4914-4921 (2015).

23   Mayorov, A. S. et al. Micrometer-scale ballistic transport in encapsulated graphene at room temperature. *Nano Lett*. **11**, 2396-2399 (2011).

24   Shcherbakov, D. et al. Raman spectroscopy, photocatalytic degradation, and stabilization of atomically thin chromium tri-iodide. *Nano Lett*. **18**, 4214-4219 (2018).

25   Skomski, R., Oepen, H. P. & Kirschner, J. Micromagnetics of ultrathin films with perpendicular magnetic anisotropy. *Phys*. *Rev*. *B* **58**, 3223-3227 (1998).

26   Christian, D. A., Novoselov, K. S. & Geim, A. K. Barkhausen statistics from a single domain wall in thin films studied with ballistic Hall magnetometry. *Phys*. *Rev*. *B* **74**, 064403 (2006).

27   Ho, J. T. & Litster, J. D. Divergences of the magnetic properties of $CrBr_3$ near the critical point. *J*. *Appl*. *Phys*. **40**, 1270-1271 (1969).

28   Vaz, C. A. F., Bland, J. A. C. & Lauhoff, G. Magnetism in ultrathin film structures. *Rep*. *Prog*. *Phys*. **71**, 056501 (2008).

29   Xu, C., Feng, J., Xiang, H. & Bellaiche, L. Interplay between Kitaev interaction and single ion anisotropy in ferromagnetic CrI_3 and $CrGeTe_3$ monolayers. *NPJ Computat. Mater*. **4**, 57 (2018).

30   Banerjee, A. et al. Neutron scattering in the proximate quantum spin liquid α-$RuCl_3$. *Science* **356**, 1055-1059 (2017).

Methods-only references

31   Liu, S. et al. Single crystal growth of millimeter-sized monoisotopic hexagonal boron nitride. *Chem*. *Mater*. **30**, 6222-622 (2018).

32   Wang, L. et al. One-dimensional electrical contact to a two-dimensional material. *Science* **342**, 614-617 (2013).

33   Ben Shalom, M. et al. Quantum oscillations of the critical current and high-field superconducting proximity in ballistic graphene. *Nat*. *Phys*. **12**, 318-322 (2016).

34   Frisenda, R. et al. Recent progress in the assembly of nanodevices and van der Waals heterostructures by deterministic placement of 2D materials. *Chem*. *Soc*. *Rev*. **47**, 53-68 (2018).

35   Novoselov, K. S. et al. Submicron probes for Hall magnetometry over the extended temperature range from helium to room temperature. *J*. *Appl*. *Phys*. **93**, 10053-10057 (2003).

Author contributions

M.K. and P.K. carried out the project and analysed the experimental data. A.K.G. suggested and supervised the project. P.K., J.B. and S.G.X. fabricated devices. M.K., A.I.B. and W.K. performed electrical and SQUID measurements. D.G.H. and S.H. provided TEM analysis. M.K. performed the finite-element simulations. J.K. and P.A.M. provided theoretical support. S.L. and J.H.E. supplied hBN crystals. M.K., P.K., K.S.N., I.V.G., J.B. and A.K.G. wrote the manuscript. All the authors contributed to discussions.

**Competing interests**

The authors declare no competing interests.
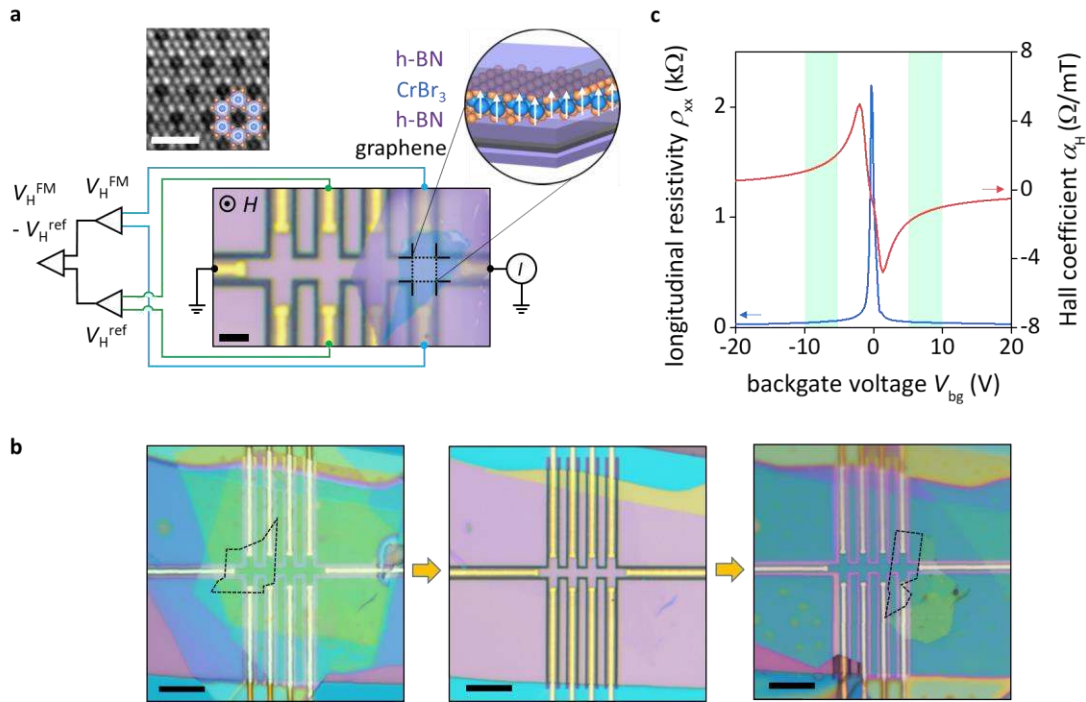
Figure 1 | Graphene-based Hall micromagnetometry. a, Optical micrograph of a graphene Hall bar with encapsulated $CrBr_3$ on top of one of the crosses. The $CrBr_3$ crystal is shown in false transparent-blue, for clarity. Scale bar, 2 µm. Our measurement circuit using three differential amplifiers is also shown schematically. The FSA is indicated by the black dotted lines. Left inset: Transmission electron micrograph of relatively thick (~10 layers) $CrBr_3$ with its molecular model in the corner. Blue and orange balls denote Cr and Br atoms, respectively. Scale bar, 1 nm. Right inset: Schematic cross-section of the vdW heterostructure. White arrows: spins in monolayer $CrBr_3$. **b,** Reusability of the Hall magnetometers. An encapsulated monolayer of $CrBr_3$ is first measured (left panel), then removed (centre) and finally replaced with another encapsulated $CrBr_3$ sample (right). The positions of $CrBr_3$ monolayers are indicated by the black lines. The changes in colour come from not only the 2D ferromagnets but also a finite thickness of encapsulating hBN that cover large areas. Scale bar, 10 µm. **c,** Examples of ρ_{xx} and α_H as a function of V_{bg} at 2 K. Green areas: Typical V_{bg} used in the magnetometry measurements.
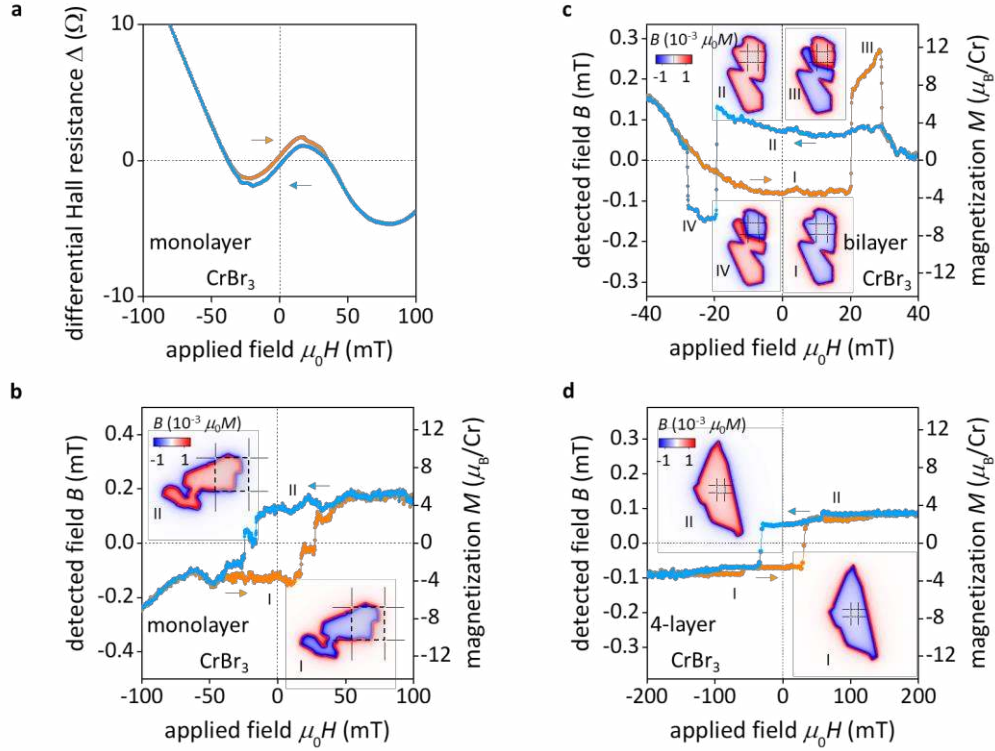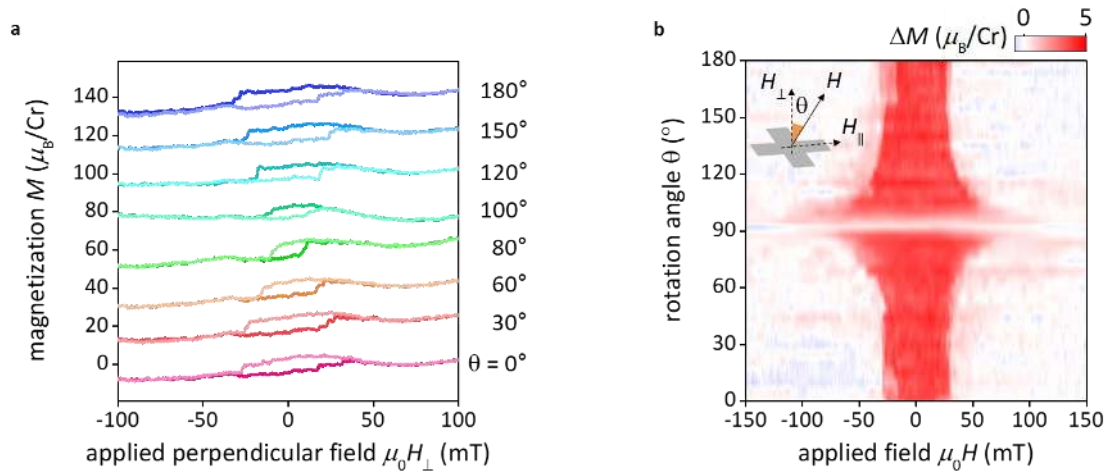
Figure 2 | Magnetic hysteresis in few-layer CrBr₃. a, Differential Hall resistance Δ for monolayer CrBr₃. It shows magnetic hysteresis at 2 K whereas the smooth background remained practically the same over a wide T range, including T above critical. **b-d,** Examples of magnetic hysteresis for mono-, bi- and four- layer CrBr₃ crystals at 2 K. Panel (b) shows the same data as in (a) but after subtraction of the T-independent background. The insets show the shape of the studied CrBr₃ crystals and their positions with respect to the FSA (black lines). The colours represent results of our numerical simulations of the perpendicular field $B(x,y)$ emanating from the 2D ferromagnets into the graphene plane. The average of $B(x,y)$ within the FSA corresponds to the experimentally detected field B. Colour bars: Proportionality coefficient between $B(x,y)$ and M for the given ferromagnets at saturation. The right y-axes are to indicate the scale for the saturation magnetization. In (c), possible positions of a domain wall with respect to the FSA are illustrated in the insets marked III and IV. Note that, to enhance the measured magnetic response, it is advantageous to position 2D ferromagnets so that their edges are close to the FSA, as in (b) rather than in (c, d). One can see from the figures that this leads to twice larger B because of weaker demagnetization effects in the former case.
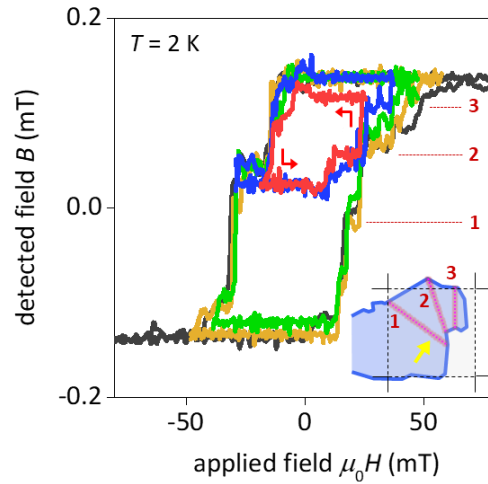
Figure 3 | Movement of domain walls in monolayer CrBr$_3$. Hysteresis loops captured by gradually decreasing the sweeping range from 100 mT (black) to 50 (dark yellow), 40 (green), 30 (blue) and 20 (red) mT. Each consecutive loop started in a positive field (for example, the 50 mT loop was recorded after H was swept from -100 mT to +50 mT, then the sweep direction was reversed and the field was swept to -50 mT, and so on). Different constant-B states correspond to different domain configurations inside the monolayer ferromagnet. Inset: One of possible scenarios for propagation of a domain wall within the FSA. The red dotted lines mark the calculated pinned wall positions, which would give the magnetization (Barkhausen) steps denoted by the corresponding numbers on the hysteresis loop. The yellow arrow indicates direction of the wall's movements.
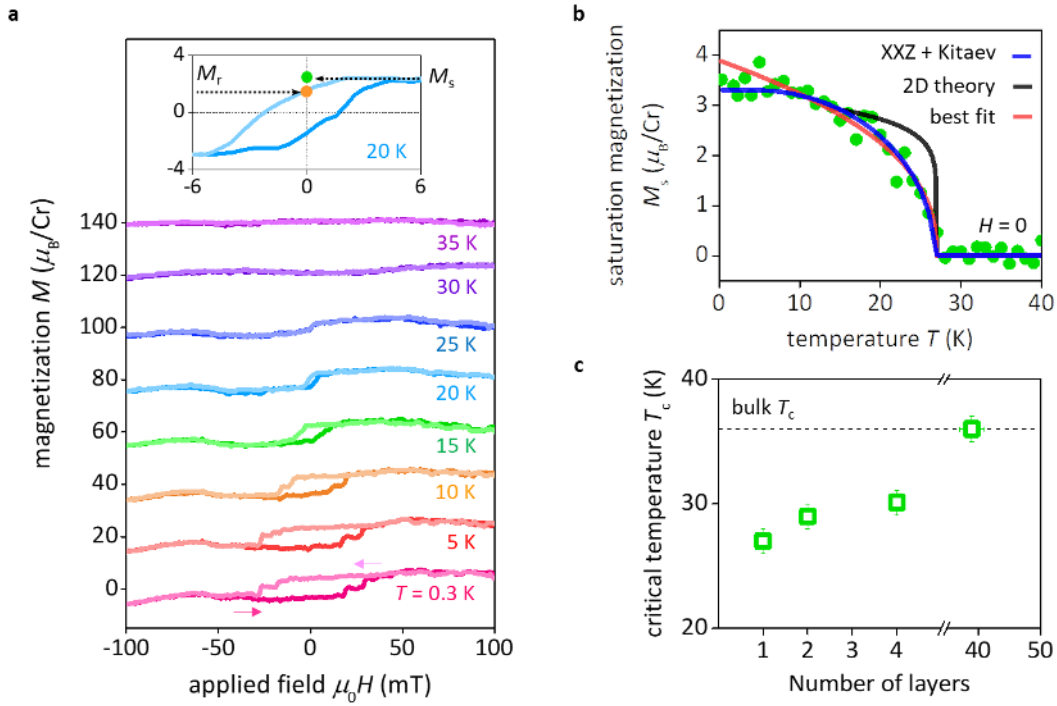
Figure 4 | Temperature dependence of ferromagnetism in 2D CrBr₃. a, Magnetic hysteresis in monolayer crystals at several representative T. Inset: Magnified coercivity loop at 20 K emphasizes the difference between remanent magnetization M_r and saturation magnetization M_s. **b**, T dependence of M_s for monolayer CrBr₃ (green symbols). The red curve is the best fit to the critical power law, yielding β ≈ 0.4. Blue curve: Mean field description using a spin-anisotropic XXZ model. Black: 2D Ising model (β = 0.125). **c**, Thickness dependence of the critical temperature. Dashed line: T_c for bulk CrBr₃. Error bars: Experimental uncertainty in determining T_c.

Figure 5 | Monolayer CrBr₃ in tilted magnetic fields. a, Hysteresis loops as a function of $H_\perp$ for several angles. **b,** Magnetic hysteresis ΔM as a function of H and θ. ΔM is defined as half the difference between sweeps recorded for plus and minus field directions. For the 90° angle, we could not detect any hysteresis because H needed to cause the magnetization switching exceeded the operational range of our magnetometers. This resulted in the white streak seen in the plot for this angle. Inset: Schematics of the rotation measurements. $T = 2$ K for both panels.